Spatial impulse response of lithographic infrared antennas

Christophe Fumeaux, Glenn D. Boreman, Werner Herrmann, Fritz Kurt Kneubühl, and
Hugo Rothuizen

We present measurements of the spatial response of infrared dipole and bow-tie lithographic antennas. Focused 10.6-μm radiation was scanned in two dimensions across the receiving area of each antenna. Deconvolution of the beam profile allowed the spatial response to be measured. The in-plane width of the antenna's spatial response extends approximately one dielectric wavelength beyond the metallic structure. Determination of an antenna's spatial response is important for several reasons. The power collected by the antenna can be calculated, if the collection area and the input irradiance (watts per square centimeter) are known. The actual power collected by the antenna is required for computation of responsivity and noise-equivalent power. In addition, the spatial response provides insight into the current-wave modes that propagate on an antenna and the nature of the fringe fields that exist in the adjacent dielectric. © 1999 Optical Society of America

OCIS codes: 040.0040, 040.1880, 040.3060, 040.5160, 040.5570.

1. Introduction

Far-infrared and millimeter-wave receiving systems often use planar antennas to facilitate efficient coupling of radiation to subwavelength-sized detectors.[1] Sensors that operate in the thermal infrared (IR) portion of the spectrum can be made with ultrafast response times (as short as tens of femtoseconds).[2] To achieve these response times, the sensors must be considerably smaller than the wavelength, and thus antennas are required for efficient coupling of the radiation into the sensor. Antenna-coupled IR sensors have been demonstrated near 10 μm with various types of detectors, including thin-film metal–oxide–metal (MOM) diodes,[3–7] and Nb microbolometers.[8]

Antennas are typically characterized with collimated radiation to find their far-field angular response pattern,[9] which is the directivity $D(\theta, \phi)$. However, we use a focused beam to measure the near-field spatial response of lithographic dipole and bow-tie antennas at 10.6 μm. We scan a normally incident focused spot across the receiving area of the antenna in the along-arm and the cross-arm directions to measure the width of the antenna's spatial response in the two principal directions. The effective collection area $A_e(\theta, \phi)$ and the directivity $D(\theta, \phi)$ are related as follows[9]:

$$A_e(\theta, \phi) = \frac{\lambda^2}{4\pi} \eta D(\theta, \phi), \tag{1}$$

where η is the radiation efficiency of the antenna and λ is wavelength.

The concept of the effective collection area is relevant for antenna-coupled IR detectors, although to the best of our knowledge the literature does not report any previous experimental determination. The typical figures of merit for IR detectors, such as responsivity $\mathscr{R}$ or noise-equivalent power (NEP), require that the power collected by the detector be known for a given set of experimental conditions. Knowledge of the effective collection area allows calculation of the collected power as the product of area and incident irradiance (watts per square centimeter). The effective collection area is also an important design parameter for developing arrays of antenna-coupled IR detectors and for defining the element-to-element spacing required for efficient power collection. The spatial response function also

---

C. Fumeaux (cfumeaux@creol.ucf.edu) and G. D. Boreman (boreman@creol.ucf.edu) are with the Department of Electrical Engineering, Center for Research and Education in Optics and Lasers, University of Central Florida, Orlando, Florida 32816-2700. W. Herrmann and F. K. Kneubühl are with the Institute of Quantum Electronics, Swiss Federal Institute of Technology, Eidgenössische Technische Hochschule, CH-8093 Zürich, Switzerland. H. Rothuizen is with IBM Research Laboratory, Saümerstrasse 4, CH-8803 Ruschlikon, Switzerland. When this research was performed, C. Fumeaux was a PhD student at the Eidenössiche Technische Hochschule.

Received 2 July 1998; revised manuscript received 18 August 1998.

0003-6935/99/010037-10$15.00/0

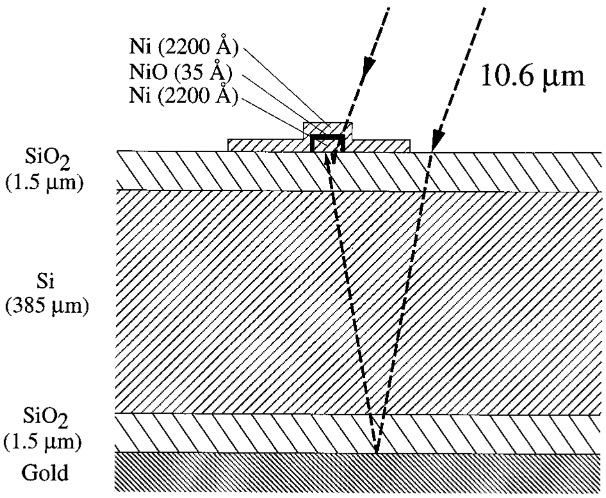

Fig. 1. Cross section of the antenna structure, showing the Ni–NiO–Ni diode, Si substrate, SiO_2 matching layers, and gold reflector.

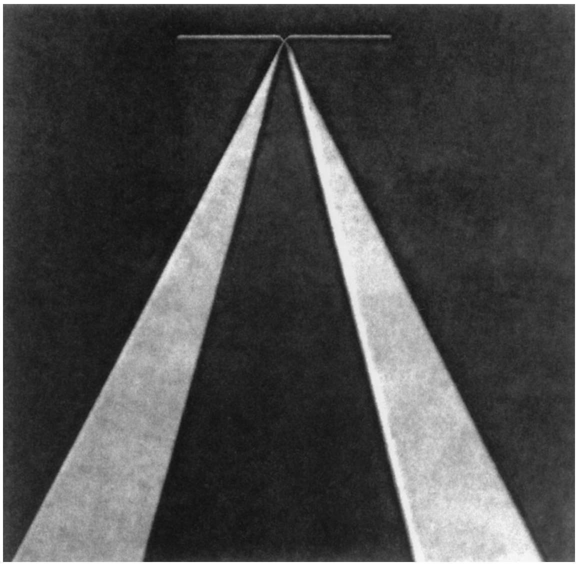

Fig. 2. Electron micrograph of an IR dipole antenna coupled to a MOM diode, showing the readout connections.

determines the amount of cross coupling seen between adjacent antennas. Electromagnetic cross talk decreases with increased antenna spacing. With a mutual-impedance calculation,[10] a closest spacing consistent with a given allowable level of cross talk between adjacent sensors can be determined. Finally, measurement of the spatial response gives insight into the current-wave modes that propagate on the lithographic antenna structure. These current distributions are difficult to model at mid-infrared frequencies because of the presence of the substrate[1] and because of the large complex component of the surface impedance.[11] Experimental determination of collection areas thus provides an important method for the verification of the results of numerical models of IR lithographic antennas.

2. Structures Measured

The first IR antennas[12] were metal whiskers with sharp, pointed ends, which were used as point-contact MOM diodes for fast detection and mixing of 10.6-μm radiation. The mechanical instability of the point-contact configuration and the difficulty of manufacturing arrays of point-contact diodes led to the development of thin-film techniques for the fabrication of MOM diodes integrated with IR antennas.[3–4,13] We previously reported development of thin-film Ni–NiO–Ni diodes as detectors and mixers of 30-THz CO_2-laser radiation,[2,4–7,14–16] for which the smallest contact areas achieved were 110 nm × 110 nm. The diodes were coupled to a variety of dipole, bow-tie, and spiral antennas. These diodes were fabricated[6] with direct-writing electron-beam lithography at the IBM Research Laboratory, Rüschlikon, Switzerland. Figure 1 shows a schematic cross section of the diode and indicates the thickness of each layer. The diodes used for the experiments described here had larger contact areas (180 nm × 180 nm) and thus had a higher power-damage threshold.

The 385-μm Si substrate was coated on both sides by 1.5-μm layers of SiO_2. These layers acted as antireflection coatings, and a 78% transmission was measured through this three-layer substrate at 10.6 μm. A gold coating was deposited onto the side of the Si wafer opposite to the antenna. Thus, as shown in Fig. 1, the radiation incident from the air side was transmitted through the substrate, reflected by the mirror, and transmitted a second time through the substrate before reaching the antenna. The reflective-coating configuration allowed optical and electrical access to the antennas from the air side, and it took advantage of the fact that a lithographic antenna receives radiation more efficiently from the substrate side than from the air side.[17]

According to transmission-line theory, the effective wavelength λ_{eff} of the current waves propagating on an antenna is determined with the effective relative electric permittivity $\varepsilon_{\mathrm{eff}}$ of the structure. At 10 μm, the effective permittivity is close to its asymptotic high-frequency limit[18] that corresponds to the permittivity $\varepsilon_{\mathrm{subst}}$ of the silicon substrate. The effective wavelength can therefore be approximated by the substrate wavelength $\lambda_{\mathrm{eff}} \approx \lambda_{\mathrm{subst}} \approx 3.1$ μm.

We measured the spatial response of full-wave dipole antennas ($L/2 = 1.55$ μm) and of bow-tie antennas with three different arm lengths. Figure 2 is a photograph of a thin-film Ni–NiO–Ni diode coupled to a dipole antenna. The low-frequency electrical leads in the form of coplanar striplines are also seen. The layer structure of the contact is apparent on the electron micrograph of Fig. 3 that shows a Ni–NiO–Ni diode coupled to a lithographic bow-tie antenna with a flare angle of 60° and a half-arm length of $L/2 = 2.3$ μm. The impedance of a finite bow-tie antenna includes reactive components that depend on the length

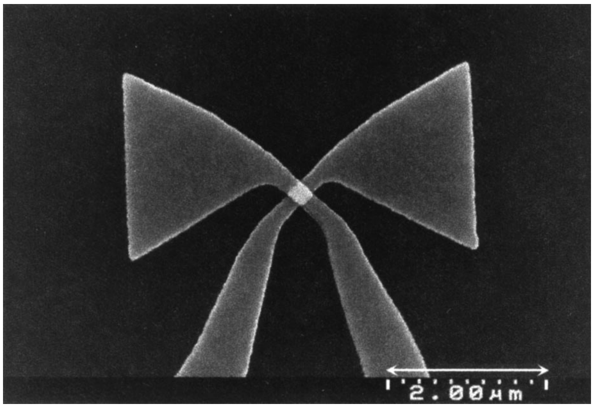

Fig. 3. Electron micrograph of an IR bow-tie antenna of total length $L = 4.6$ μm coupled to a MOM diode.

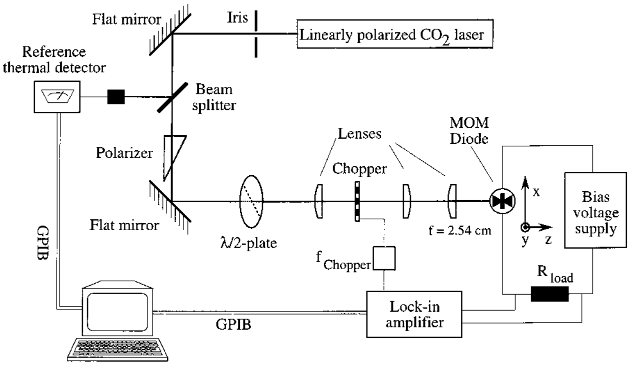

Fig. 4. Experimental apparatus for spatial-response measurement of IR antennas.

of the arms. We fabricated bow-tie antennas with three different half-arm lengths of $L/2$ equal to 1.9, 2.3, and 3.9 μm. The shortest length corresponds to the third resonance of the impedance measured by Brown and Woodward[19] for a triangular unipole in free space. The two longer bow-tie antennas have full lengths L corresponding to 3/2 and 5/2 of λ_{eff}.[20]

3. Antenna Response Versus Thermal Response

IR detection occurs in MOM diodes by at least two different mechanisms. The principal response is rectification of the terahertz-frequency current waves, which are excited in the antenna by the incident radiation. The rectification process is caused by nonlinear electron tunneling through the extremely thin oxide layer in the diode.[21] Another significant contribution to the detection signal is of thermal origin. Absorption of radiation in the SiO_2 layer of the substrate increases the temperature of the MOM diode, causing emission of thermally excited electrons over the oxide's potential-energy barrier. These two distinct detection processes combine to produce the total detected signal, but they exhibit different response times and different polarization dependence. The dependence of the detector signal on the polarization of the incident radiation permits an approximate distinction between the antenna-coupled response and the thermal response. Dipole and bow-tie antennas are linearly polarized with a maximum response for radiation polarized parallel to the antenna arms (P polarization). Consequently, the maximum detection voltage $V_{\max}$ is measured for P polarization and the minimum $V_{\min}$ is measured for the radiation polarized perpendicular to the antenna arms (S polarization). The total detected signal as a function of polarization angle can be accurately described[6,16] by the sum of a constant ($V_{\min}$) and a cosine-squared function with the amplitude $\Delta V = V_{\max} - V_{\min}$. The thermal contribution to the detected signal is independent of polarization.[6] Therefore the polarization-dependent contribution ΔV can be entirely attributed to the antenna coupling. However, the interpretation of the entire polarization-independent part of the signal $V_{\min}$ as caused by thermal effects is an approximation. For example, the electrical lead structure shown in Fig. 2 is expected to produce a residual antenna response for S polarization. Recently, we reported[2,15] on mixing experiments in which radiation from two CO_2 lasers was mixed and difference frequencies of as much as 176 GHz were detected with MOM diodes coupled to bow-tie antennas with $L/2 = 2.3$ μm. For difference frequencies in the gigahertz range, the thermal effects are too slow to contribute to the mixing signal, and the polarization dependence of the signal reflects the polarization response of the antenna. At 58 GHz we measured a polarization ratio $\Delta V/V_{\min}$ greater than 50, which justifies the assumption that $V_{\min}$ represents the thermal response. In the following, we therefore designate $V_{\min}$ as thermal response and ΔV as antenna response.

The thermal response $V_{\min}$ and the antenna response ΔV will have different spatial widths. According to antenna theory, the width of ΔV is expected to depend both on the antenna geometry and on the direction in which the focused beam is scanned. The spatial profile of the thermal response $V_{\min}$ should be independent of scan direction and independent of the antenna geometry.

4. Experimental Procedure

The experimental arrangement for the spatial response is shown in Fig. 4. The CO_2 laser was tuned to the $10P(20)$ transition and generated linearly polarized radiation at 10.6 μm in a Gaussian TEM_{00} mode. The beam was defined by use of an aperture of fixed dimension, which insured a constant beam diameter. A portion of the beam was directed onto a thermal detector by a beam splitter. The instantaneous laser power was recorded simultaneously with each reading of the signal level, allowing removal of power-fluctuation artifacts in the data. The polarization direction was rotated with a CdS half-wave plate. The radiation impinging on the diode was at normal incidence, and focused by a well-corrected lens of 25.4-mm focal length. Measurement of beam diameter just prior to the final focusing lens indicated an $F/1.5$ cone of radiation at a 30-mW level. The beam was chopped at a frequency of 3.6 kHz. A bias of 160 mV was

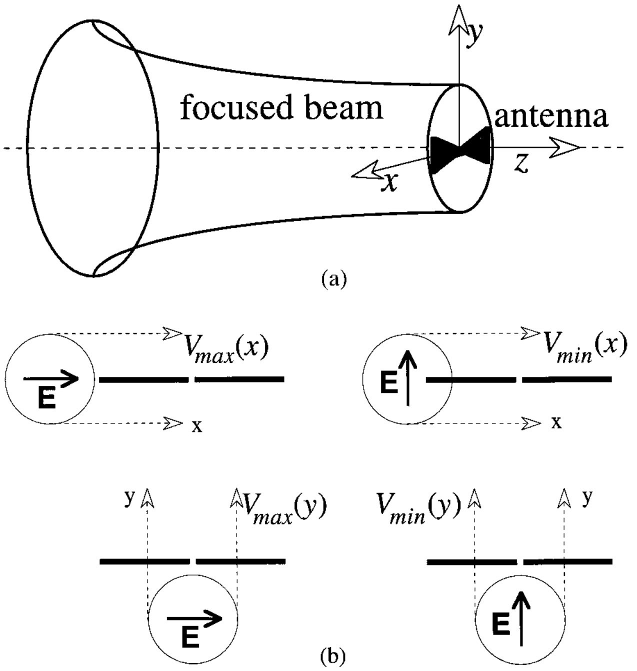

Fig. 5. (a) Scan configuration of an IR antenna in the focused laser beam. (b) Scan data $V_{\max}(x)$ and $V_{\max}(y)$ were acquired for the electric field **E** polarized parallel to the along-arm direction, whereas $V_{\min}(x)$ and $V_{\min}(y)$ were acquired with polarization in the cross-arm direction.

applied to the diode, and the ac voltage across a series resistor was measured with a lock-in amplifier.

As shown in Fig. 5(a), the antenna-coupled diode was mounted on a three-axis stage that had a positioning accuracy of approximately 1 μm. First, by use of thermally sensitive paper, the diode was approximately located at the focus. Then the precise location of the diode was adjusted along each axis to maximize the signal output, insuring that the diode was ultimately at the maximum-irradiance position of the converging beam. For each diode measured, four scans were performed, as shown in Fig. 5(b), consisting of all combinations of (x, y) scan direction and (x, y) polarization direction. We thus measured both $V_{\max}$ (using P polarization) and $V_{\min}$ (using S polarization) in the along-arm and the cross-arm directions. Data were taken at 5-μm intervals. Typical scan data (corrected for laser-power fluctuations) are seen in Figs. 6(a) and 6(b).

After data processing, each scan yielded the spatial response profile of the antenna corresponding to that combination of polarization and scan direction. The data were corrected for the incident-beam profile, as determined by the substrate-interference effects described in Section 5. The deconvolution procedure of removal of the incident-beam profile from the scan data is described in Section 6.

5. Effect of Substrate Interference on the Incident-Beam Profile

The profile of the focused laser beam was measured with a knife-edge test[22]; the knife edge was scanned in 5-μm increments along the x direction, and the transmitted power was detected with a large-area thermal detector placed behind the knife edge. The detector output as a function of x was fitted with an error function.[23] The knife-edge measurement was performed at several z locations to find the best focus. The focused beam was nearly diffraction limited, and was well described by a Gaussian with a beam waist (half-width of beam at $1/e^2$ in irradiance level) of $w_0 = 19.54$ μm.

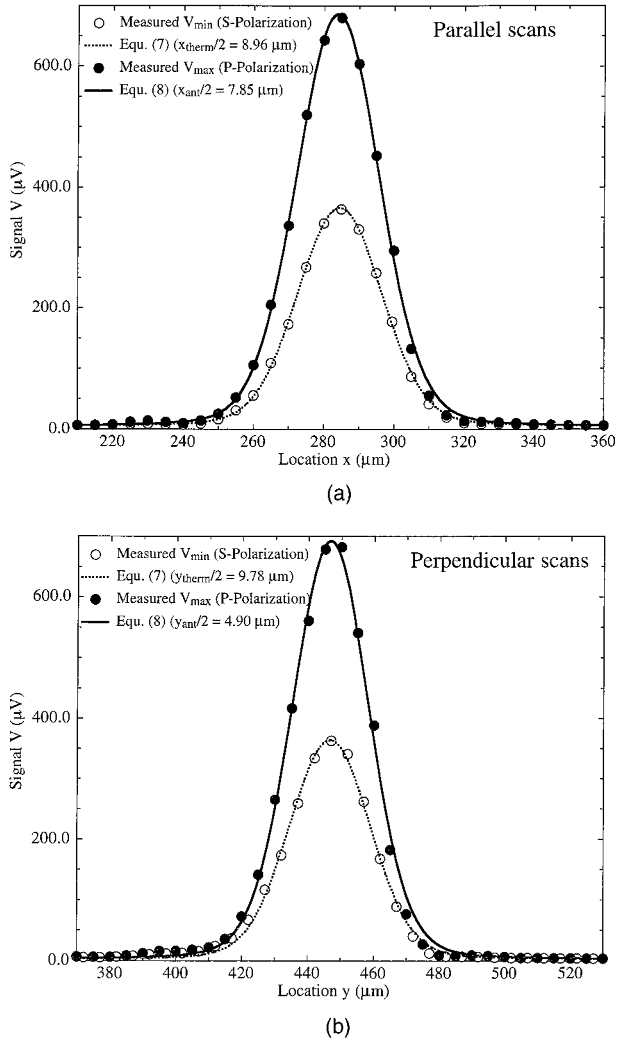

Fig. 6. (a) Typical dipole scan data for $V_{\max}(x)$ and $V_{\min}(x)$ and fitted curves corresponding to Eqs. (7) and (8), which allowed values of x_{therm} and x_{ant} to be determined. (b) Typical dipole scan data for $V_{\max}(y)$ and $V_{\min}(y)$ and fitted curves corresponding to Eqs. (7) and (8), which allowed values of y_{therm} and y_{ant} to be determined.

However, this measured beam size does not correspond to the effective input beam incident on the antenna because of substrate-interference effects. As seen in Fig. 7, the beam incident on the antenna is the coherent addition of two Gaussians, one directly incident and one that has propagated twice through the substrate (having been reflected at the gold mirror at the lower surface). Because of the low $F/\#$ of

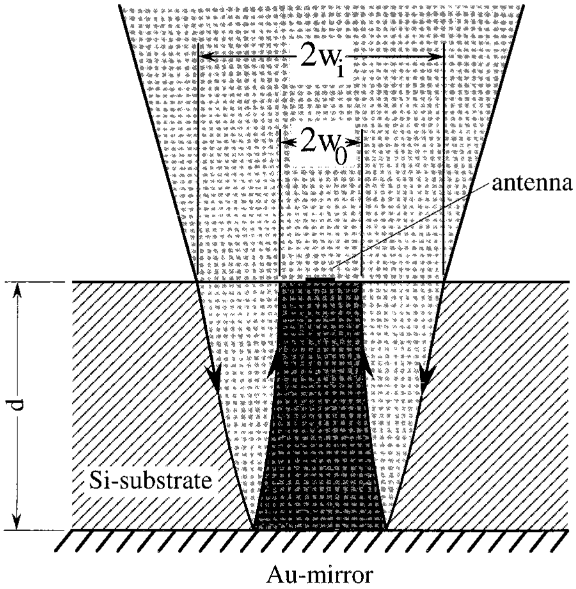

Fig. 7. Irradiance inside the substrate just below the antenna is the coherent sum of the two Gaussian beams with different widths and powers that arise from reflection at the first SiO_2–Si interface and from the gold mirror.

the final focusing lens, the two interfering beams are of different widths. A separate interferometric measurement of the substrate thickness allows us to calculate the relative phase difference Ψ_r between these two beams and, ultimately, the incident-beam irradiance on the antenna. This phase is dependent on the substrate thickness directly under the diode. The variation of substrate thickness, specified as 385 μm ± 2 μm over a 76-mm-diameter Si wafer, covers the entire range of relative phase Ψ_r from 0° to 180°, so that both constructive and destructive interference effects were seen. The variation of substrate thickness was insignificant over any particular 3 mm × 3 mm chip. Thus the relative phase was determined for each individual chip used in the experiments.

Measurement of the diode response as a function of angle of incidence θ allowed an accurate fit to be made to a two-beam interference function[7,16] from which Ψ_r was determined. For each chip, we performed this measurement for $-20° < \theta < 20°$. A typical data set measured with a dipole–antenna-coupled diode is shown in Fig. 8 with the fitted interference curve that gives the relative phase $\Psi_r = 127.32°$ for that particular chip.

The incident-beam profile was calculated as a coherent addition of an in-focus beam of power P_f, and an out-of-focus beam of lower power P_o. The waist $w_0 = 19.54$ μm of the in-focus beam corresponds to that measured by the knife-edge scan at best focus. We measured the half-width of the out-of-focus beam as $w_i = 57.73$ μm, using a knife-edge scan at a distance of 227 μm from the best-focus position. This corresponds to a phase shift equivalent to a round-trip length in the substrate, taking into account the refractive index of Si.

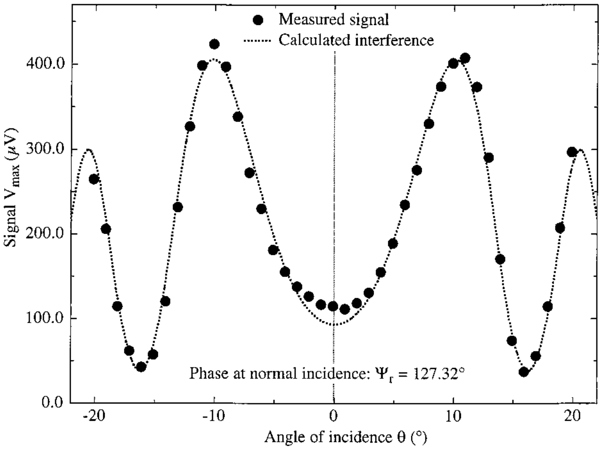

Fig. 8. Measured signal (filled circles) as a function of angle of incidence θ showing oscillations caused by substrate interference (dotted curve). Fitting the data to a two-beam interference curve allows determination of the phase $\Psi_r = 127.32°$ for the particular chip.

The magnitude of the power ratio P_f/P_o of the two interfering beams can be inferred from the contrast of the interference patterns, seen as a function of angle of incidence in Fig. 8:

$$\frac{P_f}{P_o} = \frac{{T_{\text{subst}}}^2 (1 - S)}{R_1} \approx \frac{0.61(1 - 0.52)}{0.073} \approx 4, \tag{2}$$

where T_{subst} represents the transmission of the SiO_2–Si substrate at 10.6 μm measured with a spectrometer; R_1 is the calculated reflection coefficient of the first SiO_2 layer; and S is a coefficient describing the absorptive losses in the materials. The coefficient $S = 0.52$ in Eq. (2) was obtained empirically as an average of 30 measurements similar to that shown in Fig. 8 for nominally identical substrates.

The irradiance incident on the antenna is the coherent summation of two Gaussian beams with a phase difference Ψ_r and a power ratio given by Eq. (2). The x-domain irradiance profile through the center of the beam, $B(x)$, is given by

$$B(x) = B_1(x) + B_2(x) + 2[B_1(x)B_2(x)]^{1/2} \cos \Psi_r$$

$$\text{with } B_1(x) = B_0 \exp\left(\frac{-2(x - x_0)^2}{{w_0}^2}\right),$$

$$B_2(x) = B_0 \frac{{w_0}^2}{{w_i}^2} \frac{P_o}{P_f} \exp\left(\frac{-2(x - x_0)^2}{{w_i}^2}\right). \tag{3}$$

The profile $B(y)$ in the y direction through the center of the beam was identical. As an illustration of the method, calculated incident-beam profiles are shown in Fig. 9, corresponding to phase differences measured for diodes on two different chips: $\Psi_r = 21.28°$ and $\Psi_r = 127.32°$. It can be seen that the interference effect, as expected, increases the resultant beam irradiance for constructive interference (Ψ_r near 0°) and decreases it for destructive interference (Ψ_r near 180°). There is, however, a more subtle effect that is

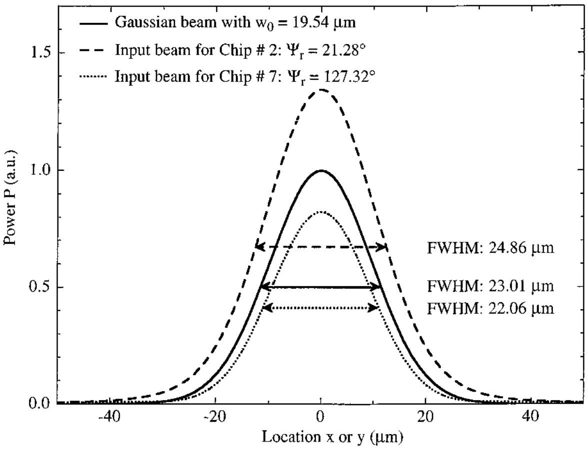

Fig. 9. Calculations of beam profile incident on the antenna with Eq. (3). The measured substrate phases for the two chips shown were $\Psi_r = 21.28°$ and $\Psi_r = 127.32°$. The plots demonstrate that constructive interference not only enhances the beam irradiance, but that it also broadens the beam profile, measured as the full width at half-maximum (FWHM). Similarly, while destructive interference decreases the beam irradiance, it also narrows the beam profile, compared with the best-focus Gaussian beam measured by the knife-edge test.

important for our measurements of the spatial impulse response. The interference also modifies the width of the resulting beam incident on the antenna. Constructive interference of a high-irradiance in-focus beam and a lower-irradiance out-of-focus beam gives a slightly broader beam, whereas destructive interference tends to narrow the beam, compared with the Gaussian profile measured with the knife-edge technique.

In summary, the spatial profile of the beam incident on the antenna is modified by a substrate-interference effect. The interference can be characterized by a relative phase between the two beams, which is a function of the local substrate thickness. This relative phase is inferred from a separate measurement of angle-dependent interference patterns for any particular chip. It is crucial to know the incident-beam profile $B(x)$, so that it can be deconvolved from the spatial-scan data to yield the spatial response of the antenna. We describe the signal-processing procedures in Section 6.

6. Data Processing

For each type of antenna investigated in this study (dipoles of $L/2 = 1.55$ μm and bow ties of $L/2$ equal to 1.9, 2.3, and 3.9 μm), we measured at least six different devices. For each device, the four required scans (x scan and y scan for both S and P polarizations) were performed with determination of the phase Ψ_r for each separate chip.

In the following, we consider for simplicity profiles in the x direction of an input beam centered at the origin, i.e., with $x_0 = 0$ μm. The calculation is identical for the y direction. The measured response of the antenna-coupled detector $h_{\text{meas}}(x)$ in the spatial domain is the convolution[24] of the impulse response $h_{\text{det}}(x)$ of the antenna-coupled detector and the effective beam irradiance profile $B(x)$ described by Eq. (3):

$$h_{\text{meas}}(x) = B(x)*h_{\text{det}}(x). \tag{4}$$

The precise functional form of the impulse response of the detector $h_{\text{det}}(x)$ is not known. For simplicity in the signal processing and interpretation, we assume an equivalent-square-width impulse response described by a rectangle function[25] for the spatial profile of the detector's thermal response as well as for the spatial profile of the detector's antenna-coupled response:

$$h_{\text{therm}}(x) = \text{rect}(x/x_{\text{therm}}), \tag{5}$$
$$h_{\text{ant}}(x) = \text{rect}(x/x_{\text{ant}}),$$

where x_{therm} and x_{ant} are the equivalent-square full widths in the x direction of the thermal and the antenna-coupled impulse responses of our detector. Using Eq. (4), we can describe the thermal response $V_{\text{min}}(x)$ by the convolution

$$V_{\text{min}}(x) = A_{1x}\int_{-\infty}^{+\infty} B(\xi)h_{\text{therm}}(x-\xi)\text{d}\xi, \tag{6}$$

where A_{1x} is a proportionality constant related to the detector's responsivity. Assuming the rect form for h_{therm}, Eq. (6) can be written

$$V_{\text{min}}(x) = A_{1x}\int_{-x_{\text{therm}}/2}^{+x_{\text{therm}}/2} B(x-\xi)\text{d}\xi. \tag{7}$$

The measured scan data $V_{\text{min}}(x)$ and $V_{\text{min}}(y)$ for the polarization perpendicular to the antenna axis [Figs. 6(a) and (b)] were numerically fitted with the functional form of Eq. (7). The free parameters of the fitting procedure were A_{1x} (or A_{1y}), x_0 (or y_0), and x_{therm} (or y_{therm}). The last pair of these parameters describes the equivalent width of the thermal impulse response of the diode. The dotted curves of Figs. 6(a) and 6(b) are examples of the evaluation of $V_{\text{min}}(x)$ and $V_{\text{min}}(y)$ fitted to Eq. (7) for the along-arm and the cross-arm scans.

The width of the detector's antenna-coupled spatial response $h_{\text{ant}}(x)$ and $h_{\text{ant}}(y)$ was determined with the profiles $V_{\text{max}}(x)$ and $V_{\text{max}}(y)$ measured for the polarization parallel to the antenna axis. Examples of these data are seen in Figs. 6(a) and 6(b). Because the thermal and the antenna signals are additive, we can describe $V_{\text{max}}(x)$ by

$$\begin{aligned} V_{\text{max}}(x) &= V_{\text{min}}(x) + \Delta V(x) \\ &= V_{\text{min}}(x) + A_{2x}\int_{-x_{\text{ant}}/2}^{+x_{\text{ant}}/2} B(x-\xi)\text{d}\xi. \end{aligned} \tag{8}$$

For each individual antenna measured, we used Eq. (7) to find the thermal response V_{min}. Using that as the first term in Eq. (8), we applied a similar fitting procedure to find $V_{\text{max}}(x)$ (or $V_{\text{max}}(y)$). The

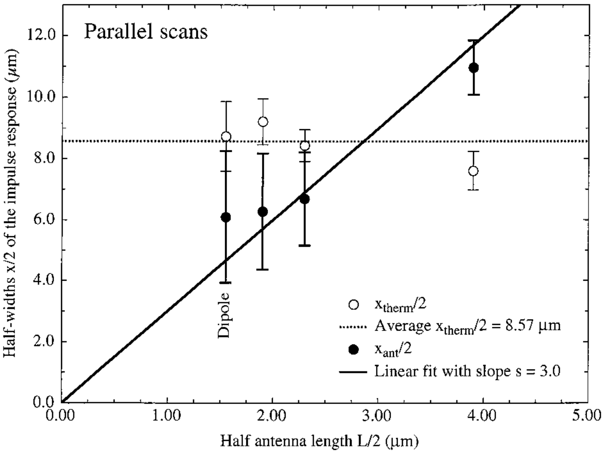

Fig. 10. Impulse-response half-widths $x_{\text{therm}}/2$ and $x_{\text{ant}}/2$ for the four types of antenna-coupled detectors measured as a function of the antenna–arm half-length $L/2$. These scans were made in the along-arm (x) direction.

fitting parameters used were A_{2x} (or A_{2y}) and x_{ant} (or y_{ant}). The results of this fitting procedure are seen as the solid curves in Figs. 6(a) and 6(b). The equivalent-square width of the spatial impulse response of the antenna in the along-arm and the cross-arm directions were found as the fitted values for x_{ant} and y_{ant}.

7. Spatial Impulse Response Results

All raw data sets for $V_{\min}(x)$, $V_{\min}(y)$, $V_{\max}(x)$, and $V_{\max}(y)$ measured for each device were processed by the procedures described in Section 6, and values of x_{therm}, x_{ant}, y_{therm}, and y_{ant} were determined for each device. These results were then averaged with similar measurements performed on at least six different devices with identical antennas to determine the mean and the standard deviation of the thermal and the antenna spatial-impulse-response widths for each antenna design. Figure 10 shows $x_{\text{ant}}/2$ and $x_{\text{therm}}/2$ plotted as a function of $L/2$ for scans made in the along-arm direction. Figure 11 shows $y_{\text{ant}}/2$ and $y_{\text{therm}}/2$ plotted as a function of $L/2$ for scans made in the cross-arm direction. The smallest antenna half-length of $L/2 = 1.55$ μm corresponds to measurements performed with the full-wave dipoles. The data for the antenna half-lengths of $L/2$ equal to 1.9, 2.3, and 3.9 μm were measured for diodes with integrated bow-tie antennas. The standard deviations are indicated by error bars in Figs. 10 and 11. The standard deviations are larger for the antenna spatial response than for the thermal response. This is expected because a calculation of the thermal response involves only $V_{\min}$, whereas a calculation of the antenna response requires measurement data for both $V_{\max}$ and $V_{\min}$. Another effect that contributes to variability in the calculated width of the antenna response is that the antenna response is much narrower than the input beam used to make the measurement scans. The deconvolution process is sensitive to small variations in the fitted width of $V_{\max}$. We found that measurements made at intervals of one month on identical devices produced resulting widths that were well within the error bars shown for both the thermal and the antenna response. Thus the error bars are consistent with both the short-term and the long-term reproducibility of our measurements.

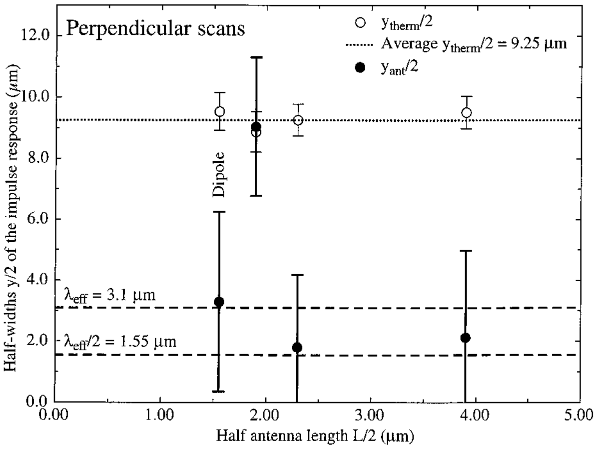

Fig. 11. Impulse-response half-widths $y_{\text{therm}}/2$ and $y_{\text{ant}}/2$ for the four types of antenna-coupled detectors measured as a function of the antenna-arm half-length $L/2$. These scans were made in the cross-arm (y) direction.

We also verified the validity of the interference-correction procedures by using Eq. (3) to find the effective input beam at the location of the antenna. We performed two sets of measurements with full-wave dipoles located on two chips exhibiting slightly different substrate thicknesses corresponding to the relative phases $\Psi_r = 21.28°$ and $\Psi_r = 127.32°$ (Fig. 9). The fitting procedures of Eqs. (7) and (8) applied to the two measurements yielded results for the antenna impulse-response width that agreed to within 1 μm.

In addition, using other functional forms for the spatial impulse response, such as Gaussians, we tried our fitting procedures and found that although similar trends were seen as those presented in Figs. 10 and 11, the use of the equivalent-square-width impulse response resulted in the smallest standard deviations.

8. Discussion and Interpretation

The measurement results presented in Figs. 10 and 11 confirm that the impulse responses for the thermal and the antenna-coupled detection mechanisms have different widths. The thermal effective area is primarily determined by thermal diffusion in the substrate and depends on the substrate material and its thickness. The width of the thermal response was approximately the same for all antenna configurations and showed only a small difference between the along-arm and the cross-arm scans. The averages of all the $x_{\text{therm}}/2$ and $y_{\text{therm}}/2$ measured are plotted as dotted lines in Figs. 10 and 11, where we find that $x_{\text{therm,avg}} \approx 17$ μm and $y_{\text{therm,avg}} \approx 18.5$ μm. The narrower thermal impulse response in the along-arm direction is probably caused by a shadowing effect, because the substrate illumination is reduced under a metallic structure with a consequently smaller temperature rise. This would also explain why the along-arm thermal response is narrower for the longer bow-tie antennas, as seen in Fig. 10.

The antenna-coupled part of the sensor response has a more complex dependence on the antenna configuration and the scan direction. Figure 10 shows that increasing the physical length of the antenna arms increases the along-arm width of the antenna response. An along-arm response width equal to the arm length would be expected from standard antenna theory,[9] whereas the $L/2 = 2.3$-μm bow tie has a full response width of approximately 14 μm, and the $L/2 = 3.9$-μm bow tie has a full response width of approximately 22 μm. As seen by the solid-line plot in Fig. 10, there is an approximate factor-of-three proportionality between the physical length of the bow ties and the along-arm width of the impulse response. The $L/2 = 1.55$-μm dipole antenna has an along-arm full response width of approximately 12 μm, indicating the existence of a fringe field that extends approximately one dielectric wavelength beyond the physical ends of the metal arms.

In the cross-arm direction the full width of the spatial response y_{ant} is somewhat narrower than x_{ant}, with a fringe field that extends a distance of between one-half and one dielectric wavelength on each side of the antenna structure. Large error bars are seen for these measurements because the measured cross-arm scan profiles exhibited widths very close to the beam profile. Under these circumstances, small variations caused by electronics noise and other experimental errors had a correspondingly larger influence on the deconvolution process.

The one exception to this behavior is the 1.9-μm bow tie, which had a cross-arm response profile of approximately 9-μm half-width. Based on the numerical modeling of these bow ties, we feel that the 1.9-μm antenna is not quite long enough to resonate at the illuminating wavelength. The spatial-response characteristic of the device was apparently influenced by the configuration of the electrical leads in addition to the bow-tie structure itself. This hypothesis is supported by the observation that $V_{\max}(y)$ for this short bow tie occurred for polarizations that were not precisely horizontal.

The results of the profile measurements on our diodes connected to dipole antennas are schematically represented in Fig. 12. The receiving areas of the detector are approximated as ellipses. The collection ellipse associated with the thermal response has principal axes x_{therm} and y_{therm} and is almost circular. The collection area of the antenna is approximated by an ellipse with principal axes x_{ant} and y_{ant}. The axial ratio of this ellipse is $y_{\mathrm{ant}}/x_{\mathrm{ant}} \approx 0.54$. A theoretical calculation of the point-spread function (PSF) for a dipole–antenna-coupled detector is described in Ref. 10, wherein Fig. 3 predicted that the principal axes of the effective collection area of a dipole-coupled detector would have an axial ratio $y_{\mathrm{ant}}/x_{\mathrm{ant}} \approx 0.5$.

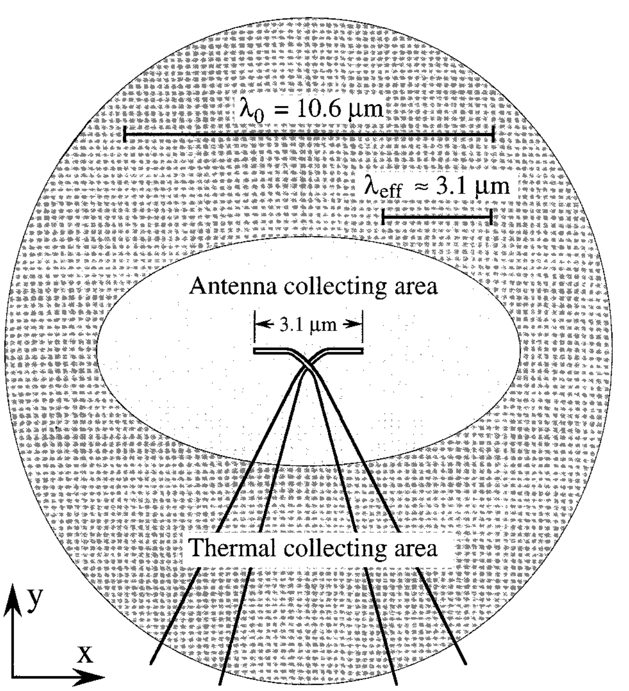

Fig. 12. Pictorial representation of the two different collection areas (antenna-coupled and thermal) measured for a dipole antenna of half-length $L/2 = 1.55$ μm. The radiation incident was at 10.6 μm with an effective wavelength inside the substrate of 3.1 μm.

9. Responsivity Results

For comparisons to be made between different devices, it is essential to know how much power from the radiation field was collected by the sensor. The determination of the collection areas of our antennas allows the calculation of the received power for a given sensor-plane irradiance E (watts per square centimeter). This parameter is crucial for quantitative radiometric comparison of the collection efficiency of different IR-antenna designs. Collected power is also a required quantity for the computation of responsivity $\mathcal{R}$ (volts per watt) and NEP (watts). The antenna collection area depends only on the antenna geometry, whereas the responsivity depends on specific sensor parameters such as the contact area of the detector, the impedance matching between the sensor and the antenna, and the substrate-interference effects.

We calculate the responsivity $\mathcal{R}$ of our antenna-coupled detectors based on the collection areas A_{coll} of the thermal and the antenna responses for each antenna design, as seen in Table 1, which were computed as the areas of ellipses with the principal axes x_{therm}, y_{therm}, x_{ant}, and y_{ant}. We also use data from Ref. 16, wherein diodes with contact areas of 140 nm × 140 nm were measured for an input irradiance $E_{\mathrm{in}} = 500$ W/cm^2. The same four antenna designs (full-wave dipoles and three different bow-tie lengths) used in the present research were used in

Table 1. Collection Areas A_{coll} of the Thermal and Antenna-Coupled Responses for Each Antenna Type[a]

Antenna type	Thermal A_{coll} ($\mu\mathrm{m}^2$)	Antenna A_{coll} ($\mu\mathrm{m}^2$)	$\overline{V_{\min}}$ (μV)	($\overline{\Delta V}$ (μV)	$\mathcal{R}_{\mathrm{therm}}$ (V/W)	$\mathcal{R}_{\mathrm{ant}}$ (V/W)
Dipole $L/2 = 1.55$ μm	261.4	63.1	125.0	119.0	0.096	0.38
Bow tie $L/2 = 1.9$ μm	256.6	178.1	160.2	135.6	0.125	0.15
Bow tie $L/2 = 2.3$ μm	245.2	38.0	152.2	245.8	0.124	1.29
Bow tie $L/2 = 3.9$ μm	227.4	73.0	140.0	88.4	0.123	0.24

[a] Also shown are the mean thermal ($\overline{V_{\min}}$) and antenna-coupled ($\overline{\Delta V}$) signal voltages, averaged over at least five different devices for each antenna type (Ref. 16). The thermal and the antenna-coupled responsivities $\mathcal{R}$ are also shown.

Ref. 16, where voltage-response measurements were made for at least five devices of each antenna design. The averaged signals $\overline{V_{\min}}$ (V_{out} for the thermal response) and $\overline{\Delta V}$ (V_{out} for the antenna response) from Ref. 16 are also given in Table 1. Knowing the irradiance conditions, the measured voltage response of the diodes, and the collection areas allows calculation of the responsivity $\mathcal{R}$ of the different antenna-coupled sensors:

$$\mathcal{R}[V/W] = \frac{V_{\mathrm{out}}[V]}{E_{\mathrm{in}}[W/\mathrm{cm}^2] \times A_{\mathrm{coll}}[\mathrm{cm}^2]}. \tag{9}$$

The data in Table 1 demonstrate that the thermal responsivity does not depend on the specific antenna type and that it is in the range of 0.1 V/W. The antenna-coupled responsivities presented in Table 1 show a strong dependence on the antenna type. They therefore permit a quantitative comparison of representative antenna-coupled IR sensors with different antenna geometries. The best responsivities (1.3 V/W) were achieved by the detectors connected to $L/2 = 2.3$-μm bow-tie antennas. Current-wave attenuation on the longer ($L/2 = 3.9$ μm) bow ties may explain their lower responsivity of 0.24 V/W. The shortest bow tie ($L/2 = 1.9$ μm) has the lowest antenna responsivity (0.15 V/W) because of a combination of the large collection area previously mentioned and a low voltage response. Dipole antennas with $L/2 = 1.55$ μm had an intermediate responsivity in the range of 0.4 V/W.

10. Conclusions

We have characterized the effective collection area of antenna-coupled IR detectors by scanning a focused laser beam across the antenna in two orthogonal directions. The response mechanism of our MOM diodes has two additive contributions originating in the rectification of antenna currents and in a thermal-detection process. The extent of the spatial response of the thermal-detection effect was nearly independent of the antenna geometry and the scan direction. Slight asymmetries in the thermal response can be explained by thermal shadowing caused by the metallic antenna structure. For the substrate configuration used in the experiments, the thermal-response region was approximately 18 μm in diameter.

The antenna-coupled collection areas are typically smaller than that for the thermal response, except for the $L/2 = 3.9$-μm bow tie, which had a full-width along-arm spatial response of nearly 22 μm. The $L/2 = 2.3$-μm bow tie had an along-arm full width of approximately 14 μm, the $L/2 = 1.9$-μm bow tie and the $L/2 = 1.55$-μm dipole both had an along-arm full width of approximately 12 μm. In general, the along-arm width of the antenna response showed approximately one dielectric wavelength of spatial response beyond the physical end of the metal arms.

In the cross-arm direction the full width of the spatial response (measured through the center of the antenna) was somewhat narrower than the along-arm response with a fringe field that extended a distance of between one-half and one dielectric wavelength on each side of the antenna structure (3- to 6-μm full width in the cross-arm direction). The only exception to this behavior was the 1.9-μm bow tie, which had a cross-arm response profile of approximately 18 μm full width, albeit at a greatly reduced responsivity. We postulate that this spatially extended low-level response was caused by spurious resonances in the antenna leads rather than in the subresonant bow-tie structure. The best antenna-coupled responsivity was measured for the $L/2 = 2.3$-μm bow tie with $\mathcal{R} = 1.3$ V/W. All of the thermal responsivities were near $\mathcal{R} = 0.1$ V/W.

An important characteristic of the antenna-coupled IR detectors is their narrow spatial-response profiles (acting nearly as point receivers), compared with Lambertian receivers of IR radiation. The sensors essentially respond to irradiance, and the use of low $F/\#$ systems is indicated to achieve the smallest diffraction spot size, which (although the focused spot will still be larger than the antennas themselves) will provide the highest possible irradiance. The small collection areas of these sensors suggest applications in oversampled IR focal plane arrays as well as in beam-profiling instrumentation. Area receivers will probably be constructed of closely spaced small arrays of antenna-coupled IR sensors with closer spacing in the cross-arm direction to ensure efficient power collection.

The authors are greatly indebted to H. Melchior, Swiss Federal Institute of Technology, Eidgenössische Technische Hochschule (ETH) Zürich; P. Vettiger and G. Sasso, IBM Research Laboratory, Rüschlikon, Switzerland; F. Heiniger, Swiss Defense Procurement Agency (GR/EMD), Bern, Switzerland; and I. Wilke, University of Hamburg, for active support and advice. This study was supported by GR/EMD, Bern; Swiss Federal Institute of Technology (ETH), Zürich; and IBM Research Laboratory, Rüschlikon. G. D. Boreman also acknowledges the support of the Ballistic Missile Defense Organization.

References

1. D. B. Rutledge, D. P. Neikirk, and D. P. Kasilingam, "Integrated-circuit antennas," in *Infrared and Millimeter Waves,* K. J. Button, ed. (Academic, New York, 1983), Vol. 10.
2. C. Fumeaux, W. Herrmann, F. K. Kneubühl, H. Rothuizen, B. Lipphardt, and C. Weiss, "Nanometer thin-film Ni-NiO-Ni diodes for mixing 28 THz CO_2-laser emissions with difference frequencies up to 176 GHz," Appl. Phys. B **66,** 327–332 (1998).
3. J. G. Small, G. M. Elchinger, A. Javan, A. Sanchez, F. J. Bachner, and D. L. Smythe, "AC electron tunneling at infrared frequencies: thin-film M-O-M diode structure with broad-band characteristics," Appl. Phys. Lett. **24,** 275–279 (1974).
4. E. Wiesendanger and F. K. Kneubühl, "Thin-film MOM-diodes for infrared detection," Appl. Phys. **13,** 343–349 (1977).
5. I. Wilke, W. Herrmann, and F. K. Kneubühl, "Integrated nanostrip dipole antennas for coherent 30 THz infrared radiation," Appl. Phys. B **58,** 87–95 (1994).
6. I. Wilke, Y. Oppliger, W. Herrmann, and F. K. Kneubühl, "Nanometer thin-film Ni-NiO-Ni diodes for 30 THz radiation," Appl. Phys. A **58,** 329–341 (1994).
7. C. Fumeaux, G. D. Boreman, W. Herrmann, H. Rothuizen, and F. K. Kneubühl, "Polarization response of asymmetric-spiral infrared antennas," Appl. Opt. **36,** 6485–6490 (1997).
8. E. N. Grossman, J. E. Sauvageau, and D. G. McDonald, "Lithographic spiral antennas at short wavelengths," Appl. Phys. Lett. **59,** 3225–3227 (1991).
9. J. D. Kraus, Antennas, 2nd ed. (McGraw-Hill, New York, 1988).
10. G. D. Boreman, A. Dogariu, C. Christodoulou, and D. Kotter, "Modulation transfer function of antenna-coupled infrared detector arrays," Appl. Opt. **35,** 6110–6114 (1996).
11. D. B. Rutledge, S. E. Schwarz, and A. T. Adams, "Infrared and submillimeter antennas," Appl. Phys. **18,** 713–729 (1978).
12. L. O. Hocker, D. R. Sokoloff, V. Daneu, A. Szoke, and A. Javan, "Frequency mixing in the infrared and far-infrared using a metal-to-metal point contact diode," Appl. Phys. Lett. **12,** 401–402 (1968).
13. S. Y. Wang, T. Izawa, and T. K. Gustafson, "Coupling characteristics of thin-film metal-oxide-metal diodes at 10.6 μm," Appl. Phys. Lett. **27,** 481–483 (1975).
14. C. Fumeaux, W. Herrmann, H. Rothuizen, P. De Natale, and F. K. Kneubühl, "Mixing of 30 THz laser radiation with nanometer thin-film Ni-NiO-Ni diodes and integrated bow-tie antennas," Appl. Phys. B **63,** 135–140 (1996).
15. C. Fumeaux, W. Herrmann, F. K. Kneubühl, H. Rothuizen, B. Lipphardt, and C. O. Weiss, "Mixing of 28 THz (10.7 μm) CO_2-laser radiation by nanometer thin-film Ni-NiO-Ni diodes with difference frequencies up to 176 GHz," Infrared Phys. Technol. **38,** 393–396 (1997).
16. C. Fumeaux, W. Herrmann, F. K. Kneubühl, and H. Rothuizen, "Nanometer thin-film Ni-NiO-Ni diodes for detection and mixing of 30 THz radiation," Infrared Phys. Technol. **39,** 123–183 (1998).
17. C. R. Brewitt-Taylor, D. J. Gunton, and H. D. Rees, "Planar antennas on a dielectric surface," Electron. Lett. **17,** 729–730 (1981).
18. M. Y. Frankel, S. Gupta, J. A. Valdmanis, and G. A. Mourou, "Terahertz attenuation and dispersion characteristics of coplanar transmission lines," IEEE Trans. Microwave Theory Tech. **39,** 910–915 (1991).
19. G. H. Brown and O. M. Woodward, "Experimentally determined radiation characteristics of conical and triangular antennas," RCA Rev. **13,** 425–452 (1952).
20. R. Compton, R. McPhedran, Z. Popovic, G. Rebeiz, P. P. Tong, and D. B. Rutledge, "Bow-tie antennas on a dielectric half-space: theory and experiment," IEEE Trans. Antennas Propag. **35,** 622–631 (1987).
21. M. Heiblum, S. Wang, J. R. Whinnery, and T. K. Gustafson, "Characteristics of integrated MOM junctions at dc and at optical frequencies," IEEE J. Quantum Electron. **14,** 159–169 (1978).
22. Y. Suzaki and A. Tachibana, "Measurement of the μm sized radius of Gaussian laser beam using the scanning knife-edge," Appl. Opt. **14,** 2809–2810 (1975).
23. M. Abramowitz and I. Stegun, *Handbook of Mathematical Functions* (Dover, New York, 1968).
24. E. L. Dereniak and G. D. Boreman, *Infrared Detectors and Systems* (Wiley, New York, 1996), Chap. 13.
25. R. N. Bracewell, *The Fourier Transform and Its Applications*, 2nd ed. (McGraw-Hill, New York, 1986).